

Banner appropriate to article type will appear here in typeset article

Fully-convolutional networks for velocity-field predictions based on the wall heat flux in turbulent boundary layers

Luca Guastoni^{1,2,†}, Arivazhagan G. Balasubramanian^{1,2}, Alejandro Güemes³,
Andrea Ianiro³, Stefano Discetti³, Philipp Schlatter^{1,2}, Hossein Azizpour^{4,2}
and Ricardo Vinuesa^{1,2}

¹FLOW, Engineering Mechanics, KTH Royal Institute of Technology, Stockholm, Sweden

²Swedish e-Science Research Centre (SeRC), Stockholm, Sweden

³Aerospace Engineering Research Group, Universidad Carlos III de Madrid, Leganés, Spain

⁴Division of Robotics, Perception, and Learning, KTH Royal Institute of Technology, Stockholm, Sweden

(Received xx; revised xx; accepted xx)

Fully-convolutional neural networks (FCN) were proven to be effective for predicting the instantaneous state of a fully-developed turbulent flow at different wall-normal locations using quantities measured at the wall. In Guastoni *et al.* (2021), we focused on wall-shear-stress distributions as input, which are difficult to measure in experiments. In order to overcome this limitation, we introduce a model that can take as input the heat-flux field at the wall from a passive scalar. Four different Prandtl numbers $Pr = \nu/\alpha = (1, 2, 4, 6)$ are considered (where ν is the kinematic viscosity and α is the thermal diffusivity of the scalar quantity). A turbulent boundary layer is simulated since accurate heat-flux measurements can be performed in experimental settings, paving the way for the implementation of a *non-intrusive* sensing approach for the flow in practical applications. This is particularly important for closed-loop flow control, which requires an accurate representation of the state of the flow to compute the actuation.

Key words: turbulence simulation, turbulent boundary layers

1. Introduction

Several approaches have been proposed over the years in order to perform a reliable non-local estimation of the velocity field in wall-bounded flows. When considering linear methods, an optimal solution can be obtained using extended proper orthogonal decomposition (EPOD, Borée 2003), which is equivalent to linear stochastic estimation (LSE, Encinar & Jiménez 2019). Recent works on transfer functions (Sasaki *et al.* 2019) have highlighted the benefits of using non-linear methods. In this regard, neural-network models have shown excellent results in monitoring the instantaneous state of the flow using quantities measured at the

† Email address for correspondence: guastoni@mech.kth.se

wall. Fully-convolutional networks (FCNs) provide an accurate reconstruction of the flow field at a given wall-normal location, when highly-resolved wall-shear-stress fields are used as inputs (Guastoni *et al.* 2021). Other architectures have been tested in the literature for the same task, *e.g.* super-resolution generative adversarial networks (SR-GANs, Güemes *et al.* 2021). While it is straightforward to measure the wall-shear-stress components in direct numerical simulations (DNSs), sampling the same quantities in an experiment is much more difficult, in particular if a high resolution is required. This highlights the need of other input quantities, whose acquisition is more practical in experiments. Several examples in the literature demonstrate the feasibility of time-resolved convective heat flux measurements (Gurka *et al.* 2004; Nakamura & Yamada 2013; Mallor *et al.* 2019), hence this quantity is used by our neural-network model to reconstruct the flow field. Previously, Kim & Lee (2020) used convolutional neural networks (CNNs) to predict the instantaneous wall-normal heat flux from the two wall-shear-stress components. Their approach still relies on the knowledge of the shear stresses at the wall and both the measurements and the predictions are at the same location. In this work, on the other hand, we consider input measurements at the wall and target flow-state estimation above the wall.

Despite machine-learning-based control having been tested in experimental settings with promising results (Gautier *et al.* 2015), it is difficult to acquire from experimental facilities the large datasets that are needed to train neural network models. Additionally, experimental uncertainty needs to be taken into account and the possibility to assess the effect of the spatial resolution of the samples is limited. For these reasons, in this study, we perform the training of the networks using the data obtained from numerical flow simulations. Furthermore, the networks are trained to predict the flow using measurements that can be obtained in experiments. Thanks to this choice, the trained network models will be able to be fine-tuned on the experimental data once they are available. In future studies, we will use the methods developed here in the water tunnel facility of Universidad Carlos III de Madrid coupling time-resolved IR thermography (Raiola *et al.* 2017) with volumetric velocimetry (Discetti & Coletti 2018), to assess the feasibility of deploying this prediction framework in a practical application.

2. Dataset

The direct numerical simulation (DNS) from which the measurements and the target output fields are sampled is performed using the pseudo-spectral code SIMSON (Chevalier *et al.* 2007). While our previous work (Guastoni *et al.* 2021) focused on a fully-developed flow, namely a turbulent open-channel flow, in this work we simulate a zero-pressure-gradient (ZPG) turbulent boundary layer (TBL). The inflow condition for the velocity is a laminar profile. A random trip forcing is applied to trigger the transition to a turbulent boundary layer. A fringe forcing is applied at the outflow in order to achieve periodicity at the boundary, as requested by the solution method. Four passive scalars representing the temperature of the fluid are also simulated. We consider Prandtl number $Pr = (1, 2, 4, 6)$, indicating them with $(\theta_1, \theta_2, \theta_3, \theta_4)$, respectively. For all the passive scalar we impose an isothermal wall boundary condition $\theta_i|_{y=0} = 0$, for $i = 1, 2, 3, 4$. The highest Prandtl number $Pr = 6$ is the result of a trade-off between the value that can be measured in our experimental setting and the computational cost of simulating such a flow with a DNS. The higher the Prandtl number, the smaller the thermal boundary layer, increasing the simulation resolution required to resolve all the relevant turbulent scales. The use of the same model for different Prandtl numbers allows us to investigate how the different thermal diffusivity influences the reconstruction performance. The choice of a spatially-developing flow implies an additional degree of complexity in the predictions with respect to the previously-studied channel flow, since

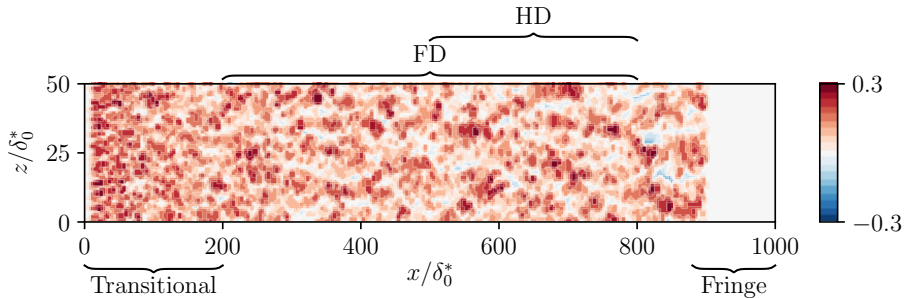


Figure 1: Representation of full domain (FD) and half domain (HD) in a sampled streamwise velocity-fluctuation field at $y^+ = 30$.

the friction Reynolds number Re_τ (based on the boundary-layer thickness and the friction velocity $u_\tau = \sqrt{\tau_w/\rho}$, where τ_w is the wall-shear stress and ρ is the fluid density) increases with the streamwise location x within the sampled fields. The highest considered Re_τ is 396, which is similar to the maximum value we expect to sample in our experimental setting. Few numerical simulation results are reported in the literature with a similar highest Prandtl number Pr and friction Reynolds number Re_τ . Alcántara-Ávila *et al.* (2021) simulated a channel flow resolving all the turbulent scales with $Pr = 6$ and $Re_\tau = 500$. Kozuka *et al.* (2009) performed a DNS of a turbulent channel flow at lower Reynolds number $Re_\tau = 395$, however, the maximum considered Prandtl number was $Pr = 7$. A statistical characterization of the scalars and the comparison with the results from the previously-cited works are available in Balasubramanian *et al.* (2023).

In our simulations, we sample the wall-shear-stress components, as well as the wall pressure. Note that we considered a reference friction velocity at the middle of the computational domain, which implies that the actual inner-scaled location that is actually sampled slightly varies along the streamwise direction. However, the variation is within $\pm 0.1y^+$. Here the '+' denotes viscous scaling, *i.e.* in terms of the friction velocity u_τ or the viscous length $\ell^* = \nu/u_\tau$ (where ν is the fluid kinematic viscosity). Furthermore, the flux of a passive scalars $\partial\theta_i/\partial y$ is sampled at the wall. The velocity-fluctuation fields (whose streamwise, wall-normal and spanwise components are denoted u , v and w , respectively) are sampled at four wall-normal locations: $y^+ = 15, 30, 50$ and 100 .

Note that the sampled fields include both the initial, transitional part of the flow and the final region affected by the fringe forcing. On the other hand, the neural-network models predict only a portion of the field. Depending on the size, we can identify two different types of samples, as shown in figure 1: *full domain* (FD) samples have streamwise and spanwise lengths of $x_s/\delta_0^* = 600$ and $z_s/\delta_0^* = 50$, respectively. Here δ_0^* is the displacement thickness of the laminar boundary layer at the inflow, defined as:

$$\delta_0^* = \int_0^\infty \left(1 - \frac{u(0, y)}{U}\right) dy, \quad (2.1)$$

with U indicating the free-stream velocity. The samples do not include the initial ($x/\delta_0^* < 200$) and the final region ($800 < x/\delta_0^* < 1000$). When the streamwise length of the samples is reduced to $x_s/\delta_0^* = 300$, we refer to them as *half-domain* (HD) samples. The grid points considered in the FD case are $N_{x,s} \times N_{z,s} = 1960 \times 320$, while for HD they are 980×320 .

In order to obtain a sufficiently large number of fields, five different realizations of the simulation are performed using five different trip-forcing random seeds. The *training dataset* includes 7,474 samples obtained from three of the five simulations. The *validation dataset*

Type	Inputs	Outputs
I	$\partial u/\partial y, \partial w/\partial y, p$	u, v, w
II	$\partial \theta_i/\partial y, \partial w/\partial y, p$	u, v, w
III	$\partial \theta_i/\partial y$	u, v, w

Table 1: Summary of inputs and outputs for different prediction types. The inputs are measured at the wall, the outputs are sampled at a given wall-normal location. The different types of predictions are performed for the four available Prandtl numbers.

consists of 2,195 samples, taken from a separate DNS to avoid unwanted correlations with the training dataset. The *test dataset* is obtained from the remaining simulation, it includes 1,973 samples and the overall sampled time for testing is sufficient to obtain converged turbulence statistics.

3. Neural network model

In this work, we consider several network architectures for different types of predictions. Based on the quantities sampled at the wall that are provided as input to the neural network, three types of predictions are investigated, as summarized in table 1.

In the first problem, a neural-network model is trained to predict the velocity-fluctuation fields farther from the wall using the streamwise and spanwise wall-shear-stress components, as well as the wall-pressure fields. The predictions of the first problem are denoted as *type I*. These predictions use the same inputs and outputs as those of our previous work (Guastoni *et al.* 2021). In the second problem, the streamwise wall-shear stress is substituted with the heat flux field corresponding to a passive scalar. We refer to these predictions as *type-II* predictions. Finally, a third problem is considered, using only the heat-flux field as input (*type III*). The latter two types of predictions are performed using all four Prandtl numbers sampled from the DNSs. Type III predictions aim to reproduce our experimental setting, in which we will be able to measure only the wall heat-flux field.

All the trained models are fully-convolutional neural networks, meaning that the input information is processed by a sequence of convolutional layers, but there are no fully-connected layers at the end, as it happens for convolutional neural networks, that are typically employed for classification tasks on the entire input. The inputs of the FCN model are normalized with the mean and standard deviation computed on the training samples. The velocity-fluctuation fields predicted by the FCN are scaled with the ratio of the corresponding root-mean-squared (RMS) values and the streamwise RMS value, following Guastoni *et al.* (2021). The scaled output quantities are indicated with \bullet .

FCNs allow an accurate reconstruction of the flow fields thanks to their capability to identify simple features and to combine them into progressively more complex ones. The FCN used as reference (Guastoni *et al.* 2021) is relatively shallow (*i.e.* few convolutional layers), with a high number of kernels per layer. On the other hand, the network architectures tested in this work have a higher number of layers with fewer kernels per layer. These modifications are designed to enhance the compositional capabilities of the model without increasing its GPU-memory footprint and computational-training cost. Note that deeper networks can be harder to train, since they are more evidently subjected to vanishing-gradient problems. Several solutions have been proposed in the literature, including but not limited to batch normalization (Ioffe & Szegedy 2015) and dropout (Hinton *et al.* 2012). We include the former in our architecture but not the latter, since dropout has been mostly used after

fully-connected layers in the literature, which are not present in our models. Additionally, it should be noted that the output of each convolutional layer is slightly smaller than the input, depending on the size of the convolutional kernel (Dumoulin & Visin 2016). When a very high number of layers is used, the output can become significantly smaller than the input. In our work, the size of the output is kept constant by modifying the size of the input field according to the architecture. This is realized by sampling a larger area in the streamwise direction and by padding periodically the field in the spanwise direction. Different models with a varying number of layers and trainable parameters are trained in order to identify the best combination of these network architecture parameters. Such comparison is performed on *type-III* predictions at $y^+ = 30$ with θ_4 heat flux as input, in an effort to optimize the network performance for its experimental use. The FCN is trained using the Adam (Kingma & Ba 2015) stochastic algorithm to minimize the mean-squared error (MSE) of the predictions with respect to the turbulent fields sampled from the DNS:

$$\mathcal{L}(\widehat{\mathbf{u}}_{\text{FCN}}; \widehat{\mathbf{u}}_{\text{DNS}}) = \frac{\sum_{i=1}^{N_{x,s}} \sum_{j=1}^{N_{z,s}} |\widehat{\mathbf{u}}_{\text{FCN}}(i, j) - \widehat{\mathbf{u}}_{\text{DNS}}(i, j)|^2}{N_{x,s} N_{z,s}}, \quad (3.1)$$

where boldface indicates the vectors containing the three velocity components and $|\bullet|$ represents the L_2 norm. We refer to the error in the individual components using $\mathcal{L}(\bullet)$ for brevity.

For *type-III* predictions, an additional auxiliary loss function is also considered: streamwise, spanwise wall-shear stress and wall-pressure field are predicted by the network as an intermediate output, in an effort to drive the internal flow representation of the FCN towards physically-meaningful and interpretable quantities.

4. Results and discussion

The quality of the network predictions is assessed using the MSE with respect to the corresponding DNS fields and the turbulence statistics accuracy. The pre-multiplied two-dimensional power-spectral densities are also computed, to assess the amount of energy reconstructed for the different scales. The comparison of the different network architectures is based on the MSE because it is the metric used to optimize the network performance during training. While increasing the number of trainable parameters in the network does not have a clear effect on the MSE, figure 2 highlights the correlation between the number of layers and the network performance for *type-III* predictions. The higher the number of layers, the lower the corresponding mean-squared error in the predictions.

The network architecture trained in Guastoni *et al.* (2021) and the deepest network in this work have roughly the same number of trainable parameters, however, the latter network shows a prediction error that is about 50% lower than the former. This result suggests higher importance of the compositional capabilities of the network over its capacity. Despite achieving the best performance in the comparison, our deepest network was not selected for the subsequent analysis primarily because of the low ratio between the output and input field size. In particular, in an experimental setting, we would not be able to increase the size of the input fields as done in this numerical investigation, hence a deeper network would inevitably result in a smaller output field in which fewer turbulent features are represented. In the remaining of this work, we present the results obtained with the second best architecture, which has about half of the layers as our deepest one, allowing to maintain a more acceptable output/input size ratio, while providing a comparable performance in terms of MSE. Note that this network has a higher number of trainable parameters, having a higher number of kernels per layer than the deepest network trained.

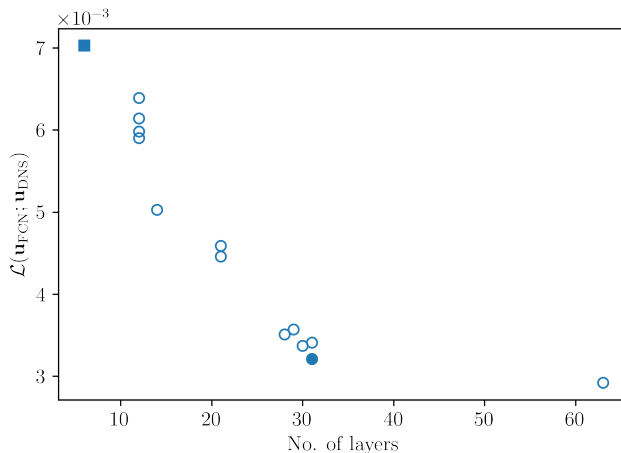


Figure 2: MSE in the predictions as a function of the number of layers of the network for *type-III* predictions, using $\partial\theta_4/\partial y|_{\text{wall}}$ as input. The filled square marker represents the network model used in Guastoni *et al.* (2021), while the filled circle is the model proposed in this work. These two latter models are compared in all the subsequent analysis.

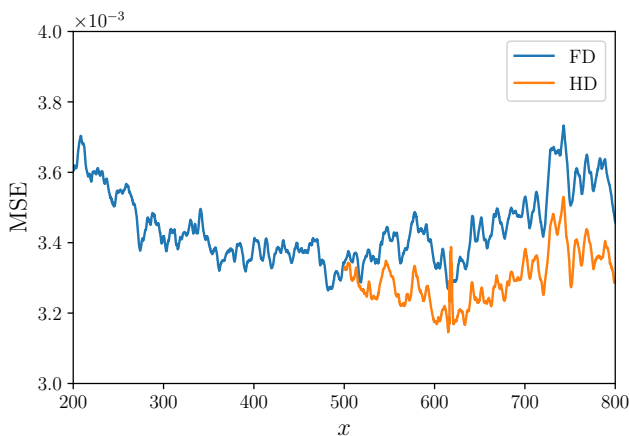


Figure 3: MSE in the predictions as a function of the streamwise location for *type-III* predictions at $y^+ = 30$. The curve represents the average over the spanwise direction and the samples in the test dataset.

Given the network architecture, the predictions on the full-domain and on the half-domain datasets are compared. One of the advantages of the FCN is that the architecture does not depend on the size of the input. Either datasets can then be used to train the neural-network model. Despite providing more information per sample during training, the predictions of the model optimized on the full-domain dataset are less accurate than the ones on the half-domain dataset. This can be explained by considering that the boundary layer is a spatially-developing flow. This means that each sample contains a range of Reynolds numbers that need to be predicted. If we consider the error in the predictions along the streamwise direction shown in figure 3, the trend exhibits a minimum at the center of the sample. This is a result of the use of MSE as training objective function. Furthermore, the larger the sample, the lower the Reynolds number at which we can achieve the highest accuracy. If we consider a smaller range

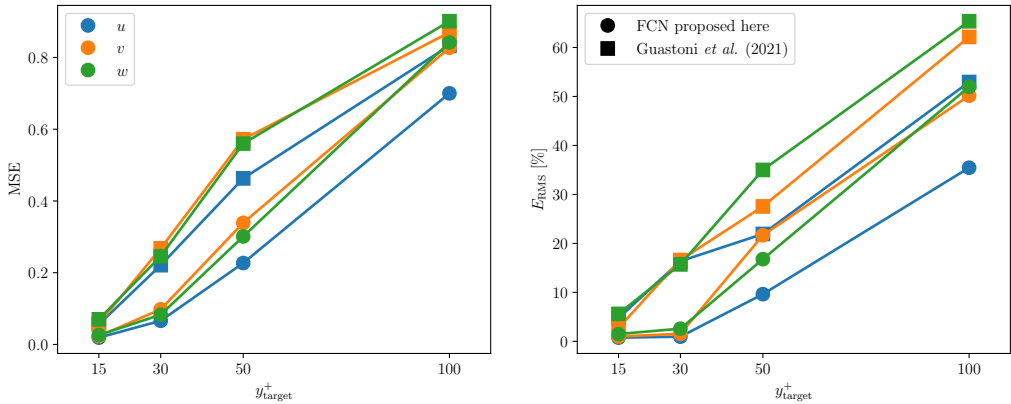


Figure 4: MSE (top) and turbulence-statistics error (bottom) obtained in *type-I* predictions with respect to target fields at different wall-normal locations. The error for each velocity component is normalized with the square of the corresponding fluctuation intensity.

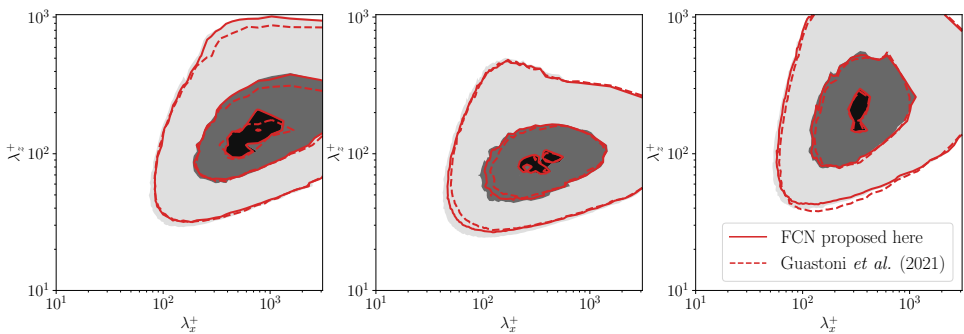


Figure 5: Pre-multiplied two-dimensional power-spectral densities for type I predictions at $y^+ = 30$. The three columns represent $k_z k_x \phi_{uu}$ (left), $k_z k_x \phi_{vv}$ (center), $k_z k_x \phi_{ww}$ (right). The contour levels contain 10%, 50% and 90% of the maximum DNS power-spectral density. Shaded contours refer to the reference data, while contour lines refer to the FCN proposed here (solid) and the network by Guastoni *et al.* (2021) (dashed), respectively.

encompassing only the higher Reynolds numbers (*i.e.* we use HD samples), more accurate predictions can be obtained at high Re . This result is encouraging for future experimental applications, since the input data that can be obtained are limited to a small interrogation window (*e.g.* obtained from particle-image velocimetry), with a small Reynolds-number range. Because of these observations, the prediction results in the subsequent part of the paper will be only related to the half-domain dataset.

Once the network architecture and the dataset are chosen, the model is trained three times, unless noted otherwise. Each training run is performed with different random initialization in order to verify the consistency of the stochastic optimizations. The reported results show the average performance of the three models. When three inputs are considered (*type-I* and *type-II* predictions), the present network is able to reconstruct the non-linear relation between input and output fields with higher accuracy than the FCN proposed in Guastoni *et al.* (2021), as shown in figure 4 (*type-I* predictions). The improvement is consistent across the entire range of investigated wall-normal locations. On the other hand, the performance degrades in a similar way as we move farther away from the wall. The accuracy of the present network at

	Type I	Type II (θ_1)	Type II (θ_2)	Type II (θ_3)	Type II (θ_4)
$\mathcal{L}(u)/u_{\text{RMS}}^2$	0.019	0.027	0.024	0.027	0.036
$\mathcal{L}(v)/v_{\text{RMS}}^2$	0.023	0.029	0.023	0.025	0.031
$\mathcal{L}(w)/w_{\text{RMS}}^2$	0.026	0.030	0.024	0.025	0.034

Table 2: Normalized MSE comparison for the different velocity components in *Type-I* and *Type-II* predictions at $y^+ = 15$. *Type-II* predictions results are shown using different scalar fields as inputs.

$y^+ = 50$ is comparable to that of the FCN in Guastoni *et al.* (2021) at $y^+ = 30$. At $y^+ = 100$, the MSE in the wall-normal and spanwise directions is similar for both architectures. The accuracy improvement is even more pronounced when considering the predicted turbulent statistics. In short, the error is lower at all y^+ locations and even at $y^+ = 100$, the current FCN performs substantially better than its predecessor. The difference in the compositional capability is evident when comparing the pre-multiplied power-spectral densities of the predictions of the two networks in figure 5. The small-scale features at $y^+ = 30$ are well predicted by both networks, however, the deeper FCN can better reproduce the larger-scale features, especially in the spanwise direction.

Type-II predictions represent an intermediate step toward the flow estimation using only the heat flux. When passing from *type I* to *type II*, the error is higher for all the velocity components, however, the streamwise component is the most affected, as shown in table 2. The heat flux at the wall is less correlated to the velocity-fluctuations away from the wall than the streamwise wall-shear stress. A higher Prandtl number for the scalar determines a higher error in the predictions, especially close to the wall. As shown in figure 6, the difference between the different scalars is less pronounced farther away from the wall. Including the spanwise wall-shear stress and the pressure as inputs makes the Prandtl dependence less evident in this type of predictions. The bottom row of figure 6 highlights an apparent inconsistency in the relation between the statistical error and the Prandtl number. Since we do not train the model for statistical accuracy directly, the error has a higher variance between models than the MSE on the individual predictions. Furthermore, only one model per Prandtl number and wall-normal location has been trained in this case. Averaging the results from different models helps retrieving the relation between the error and the Prandtl number that can be observed in the MSE. The percentual increment of the MSE due to the added difficulty of the predictions is similar for both the network proposed in this work and the one in Guastoni *et al.* (2021); note however that the predictions from the former are significantly more accurate than those of the latter. For this reason, the current FCN is found to perform better across the entire range of wall-normal locations, even for *type-II* predictions.

When *Type-III* predictions are performed, the resulting MSE is about three times higher when compared to *type-II* predictions, confirming that information in the spanwise wall-shear stress and wall pressure has an important role in the reconstruction of the fields away from the wall. Figure 7 shows how the use of a different scalar does affect the prediction quality. Close to the wall, the predictions become progressively more challenging as the Prandtl number increases. Interestingly, the difference is negligible at $y^+ = 50$ and the models trained at $y^+ = 100$ with $Pr = 4$ and $Pr = 6$ perform better than the models trained with lower-Prandtl-number inputs. Note, however, that the error in all these reconstructions is quite significant and only the largest structures are predicted. The degradation in the prediction quality with respect to the wall-normal distance was already reported in Guastoni *et al.* (2021).

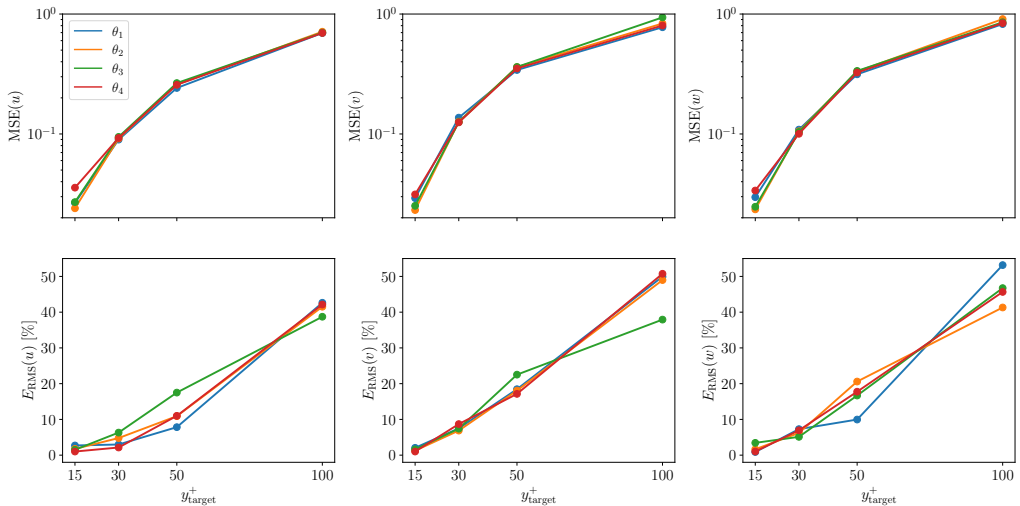


Figure 6: MSE (top) and turbulence-statistics error (bottom) obtained in *type-II* predictions with respect to target fields at different wall-normal locations, using different scalar fields as inputs. The error for each velocity component is normalized with the square of the corresponding fluctuation intensity.

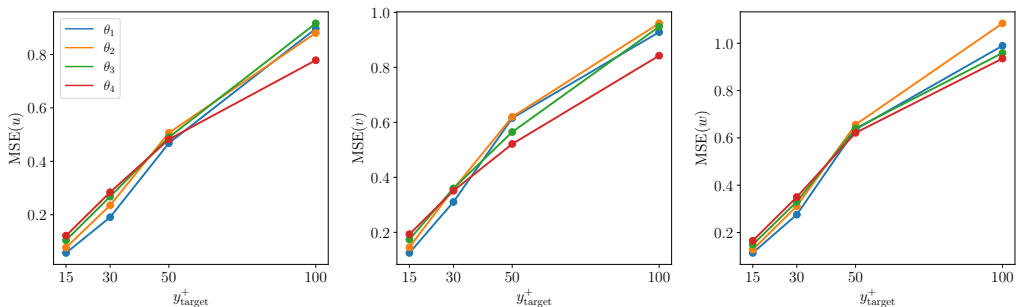


Figure 7: MSE obtained in *type-III* predictions with respect to target fields at different wall-normal locations, using different scalar fields as inputs. The error for each velocity component is normalized with the square of the corresponding fluctuation intensity.

	Guastoni <i>et al.</i>	FCN (θ_1 , no aux)	FCN (θ_2 , no aux)	FCN (θ_3 , no aux)	FCN (θ_4 , no aux)	FCN (θ_4 , aux)
$\mathcal{L}(u)/u_{\text{RMS}}^2$	0.592	0.191	0.235	0.268	0.284	0.271
$\mathcal{L}(v)/v_{\text{RMS}}^2$	0.638	0.311	0.357	0.360	0.351	0.335
$\mathcal{L}(w)/w_{\text{RMS}}^2$	0.850	0.276	0.312	0.330	0.350	0.330
$E_{\text{RMS}}(u)$ [%]	36.82 ± 0.67	7.43 ± 2.27	7.47 ± 0.90	13.61 ± 1.41	13.64 ± 2.05	11.87 ± 0.49
$E_{\text{RMS}}(v)$ [%]	39.48 ± 0.92	14.56 ± 2.39	13.16 ± 2.98	20.42 ± 1.84	22.09 ± 2.03	14.14 ± 0.93
$E_{\text{RMS}}(w)$ [%]	57.26 ± 1.24	12.31 ± 2.25	13.23 ± 2.18	18.28 ± 1.04	20.35 ± 3.25	14.04 ± 0.74

Table 3: Error comparison in *Type-III* predictions at $y^+ = 30$ using the network model from Guastoni *et al.* (2021) and the one proposed here. The variance of the statistical error is computed across the different training runs.

The statistical error for *type III* predictions can be further improved with the use of the auxiliary loss. We tested it for the predictions using $\partial\theta_4/\partial y|_{\text{wall}}$ as input: while the MSE is only about 5% lower, while the predicted turbulence statistics are up to 20% better than when the auxiliary loss function is not used, as shown in table 3. The use of an auxiliary loss function also reduces the variance between models in the statistical of all the velocity components. The error comparison with Guastoni *et al.* (2021) shows how a deeper FCN is necessary to achieve satisfactory predictions of this type. A sample *type-III* prediction at $y^+ = 30$ using the auxiliary loss function is shown in figure 8, when $\partial\theta_4/\partial y|_{\text{wall}}$ is used as input. From this figure, it is possible to observe that the FCN is able to reconstruct the large-scale features of the flow in all three velocity components starting from the heat-flux field only. The smaller-features reconstruction is less accurate, in particular, the maximum positive and negative fluctuations are typically underestimated. This is related to the use of the mean-squared error as loss function for the optimization.

We focus on the predictions whose setup is closest to the perspective experimental setting. For this, we analyze more in depth *type III* predictions using the heat flux at $Pr = 6$. A more comprehensive overview of the predicted energy at the different scales is provided by the spectra, shown in figure 9. We compare the spectra of *type-II* and *type-III* predictions at $y^+ = 30$. The amount of reconstructed energy is lower in *type-III* predictions than in *type-II*. Furthermore, it is possible to observe that eliminating the spanwise wall-shear stress and wall pressure has a higher impact on the prediction of the shorter wavelengths, both in the streamwise and spanwise direction. The accuracy reduction is more evident in the pre-multiplied wall-normal and spanwise spectra. This is expected, as the wall-pressure is well correlated with the wall-normal component of the velocity and the spanwise wall-shear stress helps to improve the prediction of the corresponding velocity-fluctuation component.

5. Conclusions

In this work, we assessed the prediction capabilities of a fully-convolutional network (FCN) using DNS data sampled from a turbulent boundary layer flow, with a maximum Reynolds number of $Re_\tau = 396$. We optimize the architecture of the FCN in order to minimize the MSE in the predictions, while maintaining a satisfactory output/input ratio of the field size. For *type II* and *type III* predictions, we describe the effect of using as input heat flux fields at progressively higher Prandtl number. Closer to the wall, the predictions become more challenging as the Prandtl number is increased. With the highest Prandtl number tested ($Pr = 6$), the resulting network yields *type-III* predictions at $y^+ = 30$ with an error that is 50% lower than that of the previously-studied architectures (Guastoni *et al.* 2021). A higher number of layers determines a larger receptive field for the network, and it enhances its compositional capabilities. The prediction accuracy is proven to be more sensitive to this parameter than the network capacity (*i.e.* the number of trainable parameters). The use of alternative, yet similar network architectures, *e.g.* ResNet by He *et al.* (2016) or UNet by Ronneberger *et al.* (2015) was only partially explored and for this reason not reported, preventing a more comprehensive analysis of the available network architectures. The use of skip connections, present in the aforementioned architectures, can potentially improve the network performance further, but this assessment is left for future work. The architectural improvements described here are essential to achieve a satisfactory velocity field reconstruction, given the additional difficulties related to the choice of a spatially-evolving flow, and the use of input quantities that are less informative than the ones used in the previous studies. In this study we limit ourselves to the *a-posteriori* analysis of the results of several trained networks, highlighting the need for deeper networks in order to obtain a satisfactory accuracy in the reconstruction. The number of layers in a network, as well as the number of trainable parameters per layer

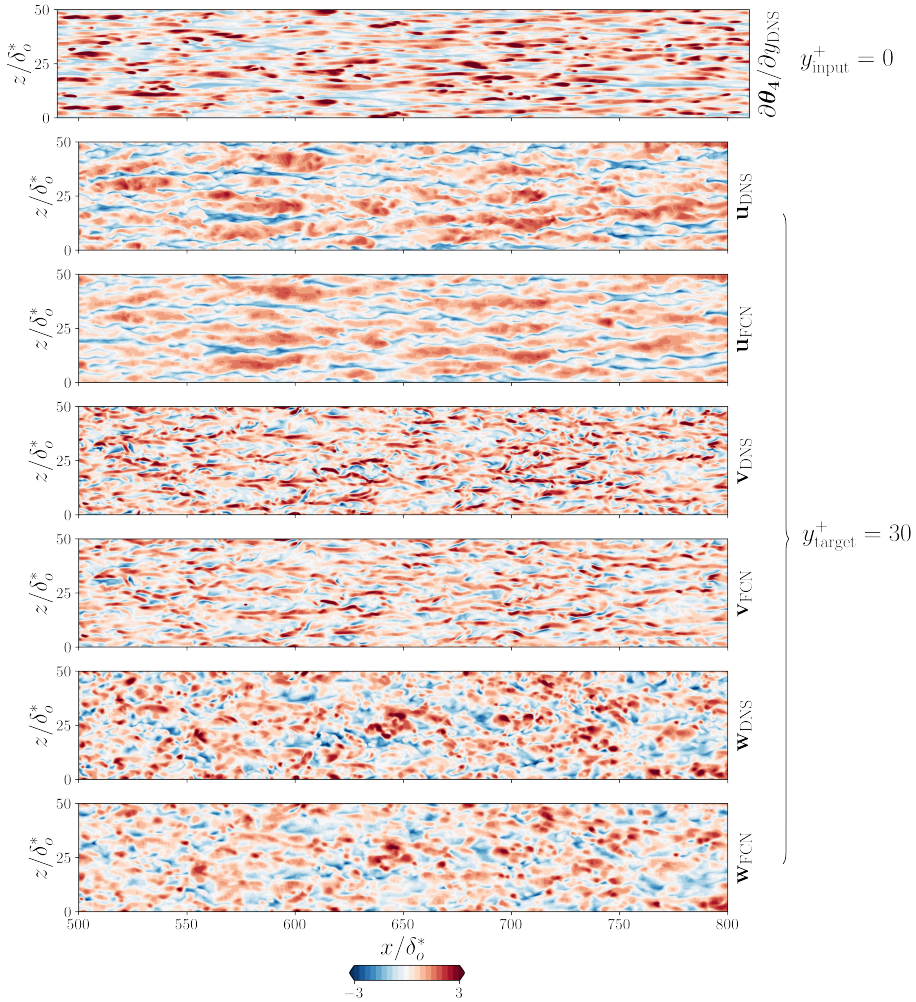


Figure 8: Sample result for *type-III* prediction at $y^+ = 30$, obtained using the proposed FCN with auxiliary loss functions. The first row corresponds to the DNS input heat flux for $Pr = 6$, normalized with the mean and standard deviation computed on the training samples. The second and third rows show the streamwise DNS velocity-fluctuation field and the corresponding prediction obtained from FCN, respectively. Similarly, the fourth and fifth rows represent the wall-normal velocity fluctuation of the target and predicted fields. Finally, the sixth and seventh rows show the spanwise velocity fluctuation component of the target and predicted fields, respectively. The velocity-fluctuation fields are scaled by the respective RMS quantities.

(e.g. the number of kernels per convolutional layer) are hyperparameters that need to be tuned to obtain the best performance of a neural network model. Automated hyperparameter searches can be conducted using evolutionary algorithms or Bayesian optimization, however, several networks still need to be trained depending on the number of hyperparameters that need to be adjusted.

After assessing the prediction capabilities of the FCN using DNS data, future work will

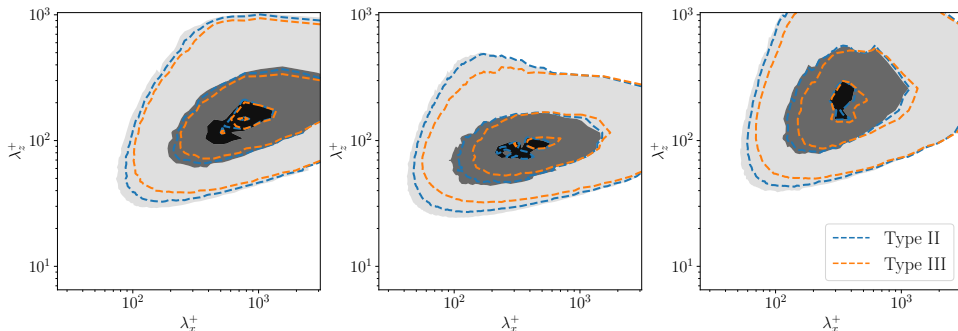


Figure 9: Pre-multiplied two-dimensional power-spectral densities of different prediction types using $\partial\theta_4/\partial y|_{\text{wall}}$ as input. The three columns represent $k_z k_x \phi_{uu}$ (left), $k_z k_x \phi_{vv}$ (center), $k_z k_x \phi_{ww}$ (right). The contour levels contain 10%, 50% and 90% of the maximum DNS power-spectral density. Shaded contours refer to the reference data, while contour lines refer to *type-II* (blue) and *type-III* (orange) predictions, respectively.

be devoted to testing the neural-network model in an experimental setting. Preliminary tests in this direction highlight the importance of the size of the input and output fields. Smaller fields tend to provide a worse reconstruction, both with numerical and experimental data. To this end, designing an experiment with the largest possible sensor size could help mitigating the penalization due to the field dimension. Furthermore, the resolution of the measured quantities is typically lower than that of DNS samples. To address this issue, a training with hybrid data should be performed: the FCN model should be first trained using DNS data aptly modified to mimic experimental data and then using samples taken directly from a wind tunnel. Testing the trained networks on this synthetic experimental data represents the next step toward the network model deployment in an experiment.

Acknowledgements. The authors acknowledge the Swedish National Infrastructure for Computing (SNIC) for providing the computational resources by PDC, used to carry out the numerical simulations.

Funding. This work is supported by the founding provided by the Swedish e-Science Research Centre (SeRC), ERC grant no. "2021-CoG-101043998, DEEPCONTROL" and the Knut and Alice Wallenberg (KAW) Foundation. S.D. and A.I. were partially supported by the project ARTURO, ref. PID2019-109717RB-I00/AEI/10.13039/501100011033, funded by the Spanish State Research Agency.

Declaration of interests. The authors report no conflict of interest.

REFERENCES

- ALCÁNTARA-ÁVILA, FRANCISCO, HOYAS, SERGIO & PÉREZ-QUILES, MARÍA JEZABEL 2021 Direct numerical simulation of thermal channel flow for $Re_\tau = 5000$ and $Pr = 0.71$. *Journal of Fluid Mechanics* **916**.
- BALASUBRAMANIAN, ARIVAZHAGAN G., GUASTONI, LUCA, SCHLATTER, PHILIPP & VINUESA, RICARDO 2023 Direct numerical simulation of a zero-pressure-gradient thermal turbulent boundary layer up to $Pr = 6$.
- BORÉE, J. 2003 Extended proper orthogonal decomposition: a tool to analyse correlated events in turbulent flows. *Exp. Fluids* **35** (2), 188–192.
- CHEVALIER, M., SCHLATTER, P, LUNDBLADH, A. & HENNINGSON, D. S. 2007 SIMSON : a pseudo-spectral solver for incompressible boundary layer flows. *Tech. Rep.*. KTH Royal Institute of Technology, Stockholm.
- DISCETTI, S. & COLETTI, F. 2018 Volumetric velocimetry for fluid flows. *Meas. Sci. Technol.* **29** (4), 042001.
- DUMOULIN, V. & VISIN, F. 2016 A guide to convolution arithmetic for deep learning. *Preprint arXiv:1603.07285*.
- ENCINAR, M. P. & JIMÉNEZ, J. 2019 Logarithmic-layer turbulence: A view from the wall. *Phys. Rev. Fluids* **4**, 114603.

- GAUTIER, N., AIDER, J.-L., DURIEZ, T., NOACK, B. R., SEGOND, M. & ABEL, M. 2015 Closed-loop separation control using machine learning. *J. Fluid Mech.* **770**, 442–457.
- GUASTONI, L., GÜEMES, A., IANIRO, A., DISCETTI, S., SCHLATTER, P., AZIZPOUR, H. & VINUESA, R. 2021 Convolutional-network models to predict wall-bounded turbulence from wall quantities. *J. Fluid Mech.* **928**, A27.
- GÜEMES, A., DISCETTI, S., IANIRO, A., SIRMACEK, B., AZIZPOUR, H. & VINUESA, R. 2021 From coarse wall measurements to turbulent velocity fields through deep learning. *Phys. Fluids* **33** (7), 075121.
- GURKA, ROI, LIBERZON, ALEX & HETSRONI, GAD 2004 Detecting coherent patterns in a flume by using piv and ir imaging techniques. *Experiments in Fluids* **37** (2), 230–236.
- HE, K., ZHANG, X., REN, S. & SUN, J. 2016 Deep residual learning for image recognition. In *2016 IEEE Conf. Comp. Vision and Pattern Recogn. (CVPR)*, pp. 770–778.
- HINTON, GEOFFREY E., SRIVASTAVA, NITISH, KRIZHEVSKY, ALEX, SUTSKEVER, ILYA & SALAKHUTDINOV, RUSLAN 2012 Improving neural networks by preventing co-adaptation of feature detectors. *CoRR abs/1207.0580*, arXiv: 1207.0580.
- IOFFE, SERGEY & SZEGEDY, CHRISTIAN 2015 Batch normalization: Accelerating deep network training by reducing internal covariate shift. *CoRR abs/1502.03167*, arXiv: 1502.03167.
- KIM, J. & LEE, C. 2020 Prediction of turbulent heat transfer using convolutional neural networks. *J. Fluid Mech.* **882**, A18.
- KINGMA, D. P. & BA, J 2015 Adam: A method for stochastic optimization. In *3rd Int. Conf. on Learning Representations, ICLR 2015, San Diego, CA, USA, May 7-9, 2015*.
- KOZUKA, MAKOTO, SEKI, YOHJI & KAWAMURA, HIROSHI 2009 DNS of turbulent heat transfer in a channel flow with a high spatial resolution. *International Journal of Heat and Fluid Flow* **30** (3), 514–524.
- MALLOR, FERMIN, RAIOLA, MARCO, SANMIGUEL VILA, CARLOS, ÖRLÜ, RAMIS, DISCETTI, STEFANO & IANIRO, ANDREA 2019 Modal decomposition of flow fields and convective heat transfer maps: An application to wall-proximity square ribs. *Experimental Thermal and Fluid Science* **102**, 517–527.
- NAKAMURA, HAJIME & YAMADA, SHUNSUKE 2013 Quantitative evaluation of spatio-temporal heat transfer to a turbulent air flow using a heated thin-foil. *International Journal of Heat and Mass Transfer* **64**, 892–902.
- RAIOLA, M., GRECO, C. S., CONTINO, M., DISCETTI, S. & IANIRO, A. 2017 Towards enabling time-resolved measurements of turbulent convective heat transfer maps with IR thermography and a heated thin foil. *Int. J. Heat Mass Trans.* **108**, 199–209.
- RONNEBERGER, O., FISCHER, P. & BROX, T. 2015 U-net: Convolutional networks for biomedical image segmentation. pp. 234–241. Springer.
- SASAKI, K., VINUESA, R., CAVALIERI, A. V. G., SCHLATTER, P. & HENNINGSON, D. S. 2019 Transfer functions for flow predictions in wall-bounded turbulence. *J. Fluid Mech.* **864**, 708–745.